



HAL
open science

Modeling the response of a top hat electrostatic analyzer in an external magnetic field: Experimental validation with the Juno JADE-E sensor

G. Clark, F. Allegrini, D. J. McComas, P. Louarn

► To cite this version:

G. Clark, F. Allegrini, D. J. McComas, P. Louarn. Modeling the response of a top hat electrostatic analyzer in an external magnetic field: Experimental validation with the Juno JADE-E sensor. *Journal of Geophysical Research Space Physics*, 2016, 121, pp.5121-5136. 10.1002/2016JA022583. insu-03669487

HAL Id: insu-03669487

<https://insu.hal.science/insu-03669487>

Submitted on 16 May 2022

HAL is a multi-disciplinary open access archive for the deposit and dissemination of scientific research documents, whether they are published or not. The documents may come from teaching and research institutions in France or abroad, or from public or private research centers.

L'archive ouverte pluridisciplinaire **HAL**, est destinée au dépôt et à la diffusion de documents scientifiques de niveau recherche, publiés ou non, émanant des établissements d'enseignement et de recherche français ou étrangers, des laboratoires publics ou privés.



Distributed under a Creative Commons Attribution - NonCommercial - NoDerivatives 4.0 International License



RESEARCH ARTICLE

10.1002/2016JA022583

Special Section:

Measurement Techniques in
Solar and Space Physics:
Particles

Key Points:

- Strong magnetic field introduces nonideal response in top hat electrostatic analyzers
- Characterized response with particle simulations and semiempirical relationships
- Validated model with experimental results from the Juno JADE-E sensor

Correspondence to:

G. Clark,
george.clark@jhuapl.edu

Citation:

Clark, G., F. Allegrini, D. J. McComas, and P. Louarn (2016), Modeling the response of a top hat electrostatic analyzer in an external magnetic field: Experimental validation with the Juno JADE-E sensor, *J. Geophys. Res. Space Physics*, 121, 5121–5136, doi:10.1002/2016JA022583.

Received 21 FEB 2016

Accepted 13 MAY 2016

Accepted article online 16 MAY 2016

Published online 2 JUN 2016

©2016. The Authors.

This is an open access article under the terms of the Creative Commons Attribution-NonCommercial-NoDerivs License, which permits use and distribution in any medium, provided the original work is properly cited, the use is non-commercial and no modifications or adaptations are made.

Modeling the response of a top hat electrostatic analyzer in an external magnetic field: Experimental validation with the Juno JADE-E sensor

G. Clark^{1,2,3}, F. Allegrini^{2,3}, D. J. McComas^{2,3}, and P. Louarn⁴

¹The Johns Hopkins University Applied Physics Laboratory, Laurel, Maryland, USA, ²Space Science and Engineering Division, Southwest Research Institute, San Antonio, Texas, USA, ³Department of Physics and Astronomy, University of Texas at San Antonio, San Antonio, Texas, USA, ⁴IRAP (Institut de Recherche en Astrophysique et Planétologie), Université Paul Sabatier de Toulouse and CNRS, Toulouse Cedex 4, France

Abstract We investigate the response function of an electrostatic analyzer when electron gyroradii in a magnetic field become comparable to the scale size of the sensor. This occurs when electrons have sufficiently small energies and are in a strong magnetic field. Through simulations and laboratory experiments with the Jovian Auroral Distribution Experiment-Electron (JADE-E) sensor, we observe the energy response, detection angle distribution, and geometric factor to change significantly. Using electro-optics simulation results, we develop semiempirical and empirical relationships that can be used for top hat electrostatic analyzers. We present a model based on these relationships that covers an energy range between 0.1 keV and 5 keV with a uniform external magnetic field magnitude between 0–3 G and verified that these relationships apply to JADE-E in a specially designed testing environment by comparing with the model. We find that the model agrees well with the JADE-E sensor validating it for top hat electrostatic analyzers more generally.

1. Introduction

Space-based electrostatic analyzers (ESAs), and similar sensors, require detailed calibrations on the ground to understand their responses before flight. Analytical [e.g., *Decreau et al.*, 1975; *Carlson and McFadden*, 1998; *Farnell et al.*, 2013] and particle trajectory methods [e.g., *Sablik et al.*, 1988; *Carlson and McFadden*, 1998; *Collinson et al.*, 2012] are used for optimizing the design. These techniques determine the main characteristics of the designs. However, they usually do not include all the complexities of a real instrument (e.g., electron scattering, residual magnetic fields, and fabrication accuracy). Differences arise from these “complexities” that are hard to predict or incorporate into the design phase [e.g., *Risley*, 1970; *Vampola*, 1998; *Clark et al.*, 2013]. As an example, Figure 1 illustrates the region of influence of three independent effects in the first-order response typically derived from the methods listed above [*Clark et al.*, 2013; *McComas et al.*, 2013]. Methods to emulate the testing environment (i.e., space or laboratory conditions), whether it is through simulation or experiment, are needed to better characterize the response. Here we focus on the electro-optical response in an ESA when electron gyroradii become comparable to the scale size (ESA radius of curvature) of the sensor. Although sometimes the magnetic field effect is assumed to be negligible [e.g., *Victor et al.*, 2006], we show through detailed experiments and simulations that the electro-optical response of an ESA can be significantly altered for low-energy electrons (≤ 5 keV) in an external magnetic field (≤ 3 G).

ESAs are commonly used to measure the energy per charge (E/q) and angular distribution of charged particles in space plasmas and elsewhere [e.g., *Young et al.*, 1998; *Pollock et al.*, 1998; *McComas et al.*, 1998; *McFadden et al.*, 2008]. Different types of ESAs (e.g., cylindrical [*Hughes and Rojansky*, 1929; *Johnstone*, 1972], toroidal [*Young et al.*, 1987], toroidal top hat [*Young et al.*, 1988], spherical [*Wolfe et al.*, 1966], spherical top hat [*Paschmann et al.*, 1985], trumpet [*Duvel et al.*, 2000], cusp [*Kasahara et al.*, 2006], and variable-radius spectrograph [*Allegrini et al.*, 2009, 2014]) all use the same principle: an electric field is produced by applying a voltage between the ESA electrodes such that charged particles are filtered by their E/q . In this study, we use data from the Juno Jovian Auroral Distribution Experiment-Electron (JADE-E) sensor [*McComas et al.*, 2013]. JADE-E consists of a set of deflector plates, a spherical top hat ESA (referred to as ESA herein), and a micro-channel plate (MCP) detector with 16 individual anodes. JADE-E’s primary objective is to explore Jupiter’s polar magnetosphere regions [*McComas et al.*, 2013; *Bagenal et al.*, 2014]. This will be done through high

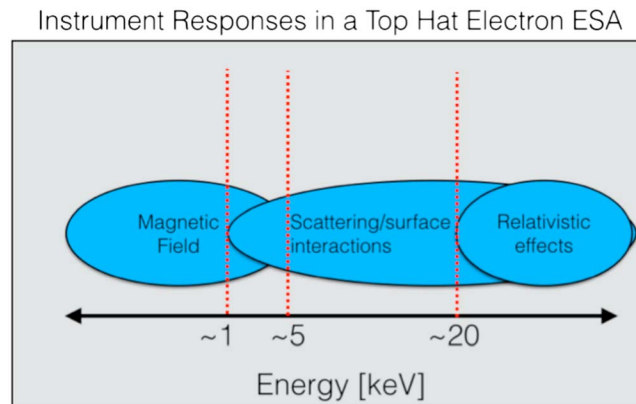


Figure 1. Responses in a top hat ESA designed to measure electrons. From left to right (increasing electron energy), the magnetic field, scattering/surface interactions, and relativistic effects play strong roles in a sensor's electro-optical properties. Red vertical bars represent approximate energy ranges. For example, magnetic field strengths on the order of a few Gauss or less can have a considerable effect on the sensor's response function for electron energies below ~ 5 keV. Electron scattering was found to be important for energies between ~ 1 keV to greater than 50 keV [Clark *et al.*, 2013]. Lastly, it was shown in McComas *et al.* [2013] that electron relativistic effects are nonnegligible for energies above 20–30 keV.

cadence (1 s) measurements of the energy and pitch angle distributions of electrons between ~ 0.1 keV and 100 keV. To track the field-aligned electrons, the deflector plates can change voltages (up to +10 kV) based on the magnetic field direction.

Typically, ESAs are designed with the assumption that the magnetic field is negligible. Instrument parameters derived under this assumption through calibration and particle simulations relate the ESA voltage and detection location to the particles incident energy and origins, respectively. However, when a strong external magnetic field is introduced, it changes the response of the ESA. What was true without magnetic field may no longer hold in the presence of a sufficiently large magnetic field. External magnetic fields have been known previously to skew the

transmission of incident particles through an ESA [Risley, 1970; Toburen and Wilson, 1977; Farnell *et al.*, 2013]; however, there has not been a detailed characterization through experiment or model.

We explored the use of a high-permeability magnetic shield [Wadey, 1956] and fabricated a cover which enclosed the sensor except for the entrance aperture. The metal successfully shielded the external magnetic field inside the sensor; however, it concentrated the field near the aperture creating a magnetic lens that distorted the information about the particle's incident energy and origin. Therefore, the benefits of a field free region inside the ESA did not outweigh the complexities introduced in the distorted field at the aperture. Thus, a magnetic shield was not used. Instead, we needed to model this effect for post analysis to determine the measured energy and pitch angle distribution as a function of electron energy, magnetic field strength, and direction. We use semiempirical relationships, which were derived from the Lorentz force, to model this response and relied on particle simulations (SIMION) [Dahl, 2000] to constrain our equations and fitting parameters. We also present results from a case study analysis with the JADE-E sensor that was tested in a specially developed laboratory facility for vacuum testing in a controlled magnetic field (documented in the appendix in McComas *et al.* [2013]).

In section 2, we describe the use of SIMION and the details of modeling this electro-optical response. In section 3, we derive the semiempirical and empirical relationships for the energy, detection angle, and geometric factor response. Section 4 presents detailed modeling results, which are used to derive the free parameters in the semiempirical equations. Section 5 compares modeling and analytical results to laboratory measurements. In section 6 we summarize and discuss the results and their implications for measuring plasma electrons in strong magnetic field environments.

2. Model

To model the response of the ESA in an external magnetic field, we use the SIMION particle trajectory simulation software [Dahl, 2000]. SIMION uses a finite-difference method to numerically solve the Laplace equation for given electrostatic and/or magnetic potential array orientation. The electrostatic potential can be computed from any given electrode geometry, thus making this software an ideal tool for modeling the response of complicated instruments. Furthermore, the ability to input a magnetic field with complete control of the orientation (in three dimensions) and magnitude makes it ideal for our study. Finally, SIMION has been shown to be an effective tool in modeling the ideal response [McComas *et al.*, 2013] and nonideal responses due to

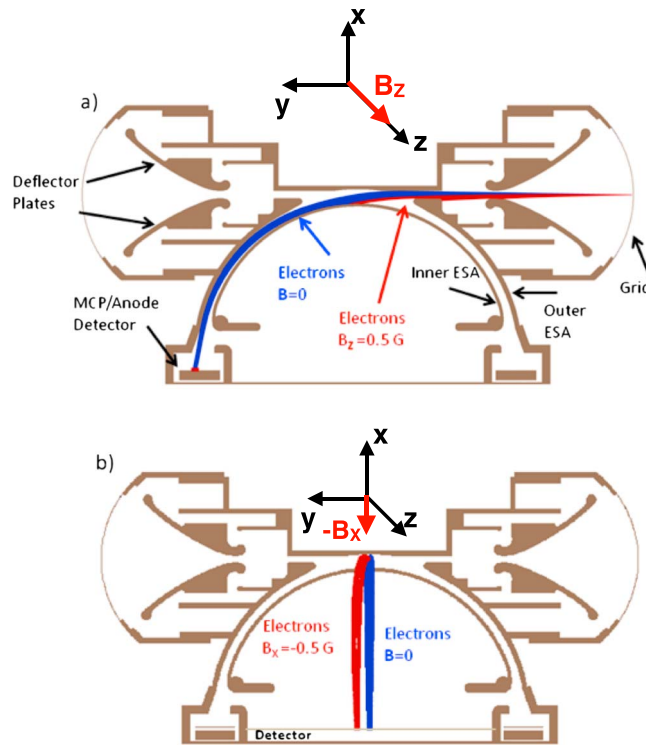


Figure 2. A 500 eV electron trajectories within the JADE-E SIMION model. Cross section of the x - y plane illustrates trajectories along the y axis with (b) $B = 0$ G (blue) or (a) $B_z = 0.5$ G (red). In Figure 2b electrons are flown along z with $B = 0$ G (blue) and $B_x = -0.5$ G (red).

section of the SIMION model. For clarity, the trajectories shown in Figure 2 only represent a small fraction of the energy, angle, and position space covered by a full simulation. In Figure 2a electrons originate at the grid and are flown along the y axis for two cases: (1) the $B = 0$ (blue trajectories) and (2) the $B_z = 0.5$ G case (red trajectories). In Figure 2b, the electrons still originate at the grid but now are flown along the z axis with the red trajectories now representing $B_x = -0.5$ G. The energy of incident electrons is approximately ~ 500 eV for this example, and the inner ESA was biased at $+55$ V. The MCP was biased at $+100$ V and a secondary electron suppressor grid (not shown) above the MCP is biased at -12 V. These are just two representative cases to illustrate the effect on the energy and detection angle response. Figure 2a illustrates the additional force along x , from $(\mathbf{v} \times \mathbf{B})\hat{x}$, which causes the electrons to strike the top of the ESA and thus are not detected. To compensate for this additional force, the ESA voltage needs to be decreased for the electrons to pass through. Similarly, in Figure 2b the $(\mathbf{v} \times \mathbf{B})\hat{z}$ force causes the electrons to be steered to a different location on the detection ring. When the force is strong enough to cause the electrons to strike an adjacent anode ($\sim 7.5^\circ$ field

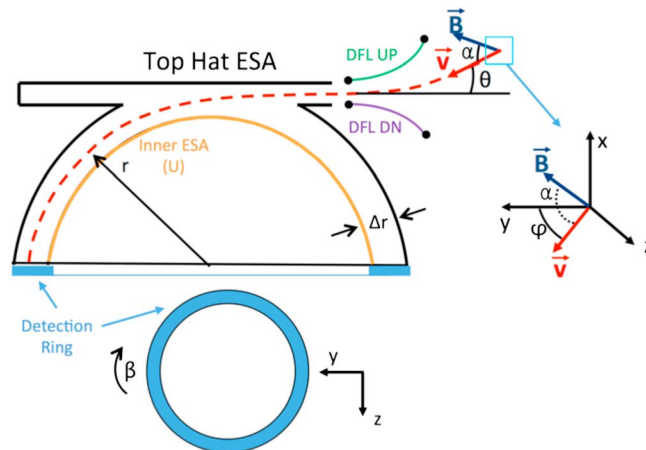


Figure 3. Schematic illustrating various components of a top hat ESA, the coordinate system, and parameters used in this study.

electron scattering [Clark et al., 2013] for the JADE-E sensor as well as other plasma sensors [e.g., Collinson et al., 2009; Randol et al., 2010].

Particle distributions are flown from the outside of the sensor, with distributions uniform in energy, angle and position covering the full transmission space. Balancing the number of particles flown and optimizing the computation time of the simulation is taken into account. Therefore, uniform distributions cover $\pm 20\%$ of the central passband energy per charge, $\pm 8^\circ$ in elevation and $\pm 15^\circ$ in azimuthal. These values were selected because the energy resolution is $\sim 10\%$ and the pixel angular and elevation coverage is $7.5^\circ \times 5^\circ$, respectively. The particles originate at the entrance grid and we fly $\sim 6 \times 10^5$ particles for each ESA voltage and magnetic field direction and magnitude. We then rotate the field direction 15° increments between 0° and 360° . In total, nearly 1.5×10^7 particles are flown.

Figure 2 illustrates the projections of electron trajectories onto a cross section of the SIMION model. For clarity, the trajectories shown in Figure 2 only represent a small fraction of the energy, angle, and position space covered by a full simulation. In Figure 2a electrons originate at the grid and are flown along the y axis for two cases: (1) the $B = 0$ (blue trajectories) and (2) the $B_z = 0.5$ G case (red trajectories). In Figure 2b, the electrons still originate at the grid but now are flown along the z axis with the red trajectories now representing $B_x = -0.5$ G. The energy of incident electrons is approximately ~ 500 eV for this example, and the inner ESA was biased at $+55$ V. The MCP was biased at $+100$ V and a secondary electron suppressor grid (not shown) above the MCP is biased at -12 V. These are just two representative cases to illustrate the effect on the energy and detection angle response. Figure 2a illustrates the additional force along x , from $(\mathbf{v} \times \mathbf{B})\hat{x}$, which causes the electrons to strike the top of the ESA and thus are not detected. To compensate for this additional force, the ESA voltage needs to be decreased for the electrons to pass through. Similarly, in Figure 2b the $(\mathbf{v} \times \mathbf{B})\hat{z}$ force causes the electrons to be steered to a different location on the detection ring. When the force is strong enough to cause the electrons to strike an adjacent anode ($\sim 7.5^\circ$ field

Table 1. Definitions and Ranges of Commonly Used Parameters in This Study

Parameter	Definition	Range/Value (in This Study)
B	Magnetic field magnitude	0–3 G
E	Electron Energy	0.1–5 keV
α	Pitch Angle	0°–180°
θ	Elevation	–30°–+30°
ϕ	Azimuth	0°–360°
β	Anode position angle	0°–360°
r	Radius of curvature	~50 mm
Δr	Gap distance	~2.5 mm
U	Voltage potential of Inner ESA	~10–550 V

of view at full width at half maximum (FWHM)), the incident direction, or pitch angle, of the incident electron could be misinterpreted.

Figure 3 represents the coordinate system graphically, and Table 1 defines all necessary parameters we use in this study. The pitch angle (α) is calculated by taking the dot product between the velocity and magnetic field vector ($\cos(\alpha) = \vec{v} \cdot \vec{B}$).

Elevation (θ) is defined in the x - y plane and azimuth (ϕ) is defined in the y - z plane. In this study, typical values of θ are between -30° to $+30^\circ$ and values of ϕ are between 0° to 360° . We also define a coordinate, β , which is the angle along the detection ring measured in the y - z plane, which varies between 0° to 360° .

3. Semiempirical Equations

3.1. Energy Equation

To make use of the results from the SIMION model, semiempirical relationships were developed. We start with the Lorentz force and balance it with the centripetal force since the electron bent along a radius curvature, r , in the ESA:

$$\vec{F} = q(\vec{E} + \vec{v} \times \vec{B}) = \frac{mv^2}{r} \tag{1}$$

where m and q are the mass and charge of the electron and \vec{E} is the electric field, which we can approximate as $\vec{E} \approx U/\Delta r$, where U is the ESA voltage potential between the spherical ESA plates (for Δr see Figure 2). Substituting the equation of \vec{E} into equation (1) and using the relationship that $\vec{v} \times \vec{B} = vB \sin\phi$ gives

$$\frac{E}{qr} = \frac{U}{2\Delta r} + \frac{vB}{2} \sin(\phi) \tag{2}$$

multiplying by r and rewriting v using the expression for an analyzer constant $\frac{1}{2}mv^2 = Uk$, where k is the analyzer constant, which can also be expressed as $k = r/2\Delta r$, which yields the following equation for the energy per charge of a particle as a function of ESA voltage, magnetic field strength, and azimuth ($E/q = (U, B, \phi)$):

$$\frac{E}{q} = Uk + r\sqrt{\frac{k}{2m}} B \sqrt{U} \sin(\phi) \tag{3}$$

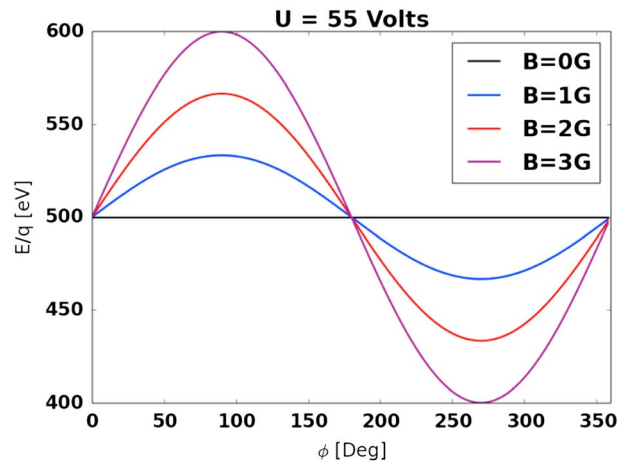


Figure 4. Energy per charge versus magnetic field azimuth for three field strengths. Black, blue, red, and purple curves represent 0, 1, 2, and 3 G, respectively. The ESA was set to 55 V.

Figure 4 illustrates equation (3) with an ESA voltage of 55 V for different magnetic field strengths as a function of ϕ . The black, blue, red, and purple curves represent the magnetic field strengths 0 G, 1 G, 2 G, and 3 G, respectively. The theoretical curves predict that for a given ESA voltage, the measured energy distribution of the incident electrons will change significantly based on the magnetic field strength and azimuth direction. First, for $B = 0$, equation (3) reduces to $E/q = Uk$, which is a well-known expression for plasma sensors [e.g., Victor et al., 2006; Allegrini et al., 2009; Collinson and Kataria, 2010].

We note that U is the optimal voltage for transmitting electrons through the ESA with kinetic energy E . For $B \neq 0$, Figure 4 shows a sinusoidal pattern with an amplitude that grows as $B\sqrt{U}$, where $r\sqrt{k/2m}$ is constant. This pattern is qualitatively consistent with the simulated trajectories in Figure 2a, where the additional force proportional to $v \times B$ bends the electrons in the ESA. The pattern in Figure 4 can also be explained by the energy-per-charge acceptance properties of the ESA. For electrons to pass through the spherical top hat portion, their equation of motion must balance the centripetal acceleration on the right-hand side of equation (1). When the magnetic field strength and direction change, the energy of the electron that satisfies this condition also changes. Realistically, there is a distribution of energies and we look into this effect in our results presented in section 4. Here this serves just as a conceptual picture for the effect of the magnetic field on the ESA's response.

Ideally, we wish to calculate a realistic energy-per-charge value based on the ESA voltage, magnetic field, and electro-optical parameters alone; however, this does not work in practice because this simple expression ignores fringe fields and other effects such as deflector voltages. Nonetheless, it provides a useful expression to analytically fit the simulation results. We can rewrite equation (3) in terms of a free fitting parameter.

$$\frac{E}{q} = Uk + C_0 B \sqrt{U} \sin(\varphi) \quad (4)$$

where C_0 replaces $r\sqrt{k/2m}$ and is determined from simulations. We note that for JADE-E, $k \approx 9$ eV/V, therefore for $U = 55$ V, $E \approx 500$ eV. Furthermore, k has been observed to change by ~ 1 eV/V ($\sim 10\%$) at electron energies near 100 keV and *McComas et al.* [2013] found that this can be modeled by including relativistic kinetic energies. We determine the relationship for C_0 as a function of energy and magnetic field strength in section 4.

3.2. Detection/Pitch Angle Response

As shown in Figure 2b the beam can be significantly deflected in azimuth (i.e., y - z plane). Here we start with a 1-D analytical approach for the force in the z direction and derive an expression that relates the pitch angle of the particle measured outside the sensor to the location it strikes on the detection ring. Then we invert the equation to have an expression for the pitch angle as a function of detection location. Again, we start with the Lorentz force, assume $\vec{E} = 0$, and write it in terms of a second order differential equation:

$$m \frac{d^2 z}{dt^2} = qvB \sin(\alpha) \quad (5)$$

z is one of the coordinates that defines the imaging plane in Figure 3 and α is the pitch angle. Solving equation (5) for z and noting that $\Delta z = (z_f - z_i)$, where final and initial values are taken to be at the detector and grid, respectively,

$$\Delta z = \frac{q}{m} \frac{\Delta t^2}{2} vB \sin(\alpha) \quad (6)$$

where Δt is the time of flight of the electron through the ESA (a 1 keV electron through JADE-E, $\Delta t \approx 1$ ns). We can relate Δz to the anode position angle (β) by letting $\Delta z = d \times \tan(\beta)$, where d is the linear distance through the ESA. Replacing this expression for Δz in equation (6) and solving for β leads to

$$\beta = \tan^{-1} \left[\frac{q}{m} \frac{vB\Delta t^2}{2d} \sin(\alpha) \right] \quad (7)$$

Noting that $\Delta t = d/v$ and $v = \sqrt{2E/m}$, we can replace the quantity $qvB\Delta t^2/2dm$ with QB/\sqrt{E} , noting that $Q = qd/\sqrt{8m}$. Finally, accounting for fact that the particle trajectory through a top hat ESA is bent $\sim 90^\circ$ by the curved electrode geometry (see Figure 3), we introduce a 90° phase shift in the sine function. Rewriting equation (7) gives

$$\beta = \tan^{-1} \left[Q \frac{B}{\sqrt{E}} \sin\left(\frac{\pi}{2} - \alpha\right) \right] \quad (8)$$

Figure 5 shows a plot of equation (8) with $U = 55$ V for various magnetic field strengths between 0 and 3 G. The black, blue, red, and purple curves represent 0, 1, 2, and 3 G. When $B = 0$, then equation (8) yields $\beta = 0$, and thus, the electrons are not deflected. When $B \neq 0$, the additional force causes the electrons to be

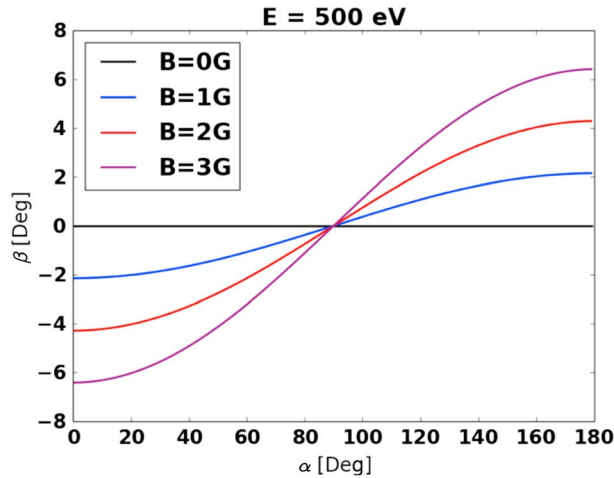


Figure 5. Detection angle on the MCP as a function of pitch angle outside the sensor. Shown are four magnetic field strengths: 0, 1, 2, and 3 G illustrated as the black, blue, red, and purple curves, respectively.

an exact solution to the electron’s detection angle through the ESA. Therefore, we added additional terms to equation (7) to account for amplitude or offset effects that are encountered. The general expression can be written as

$$\beta = A_0 \tan^{-1} \left[Q \frac{B}{\sqrt{E}} \sin \left(\frac{\pi}{2} - \alpha \right) \right] + A_1 \tag{9}$$

where A_0 represents the amplitude and A_1 is a vertical offset. We treat these as free parameters and determine the relationships as a function of energy and magnetic field strength in section 4.

4. Modeling Results

In section 3 we derived general expressions for the energy and detection/pitch angle responses of a top hat ESA in a strong external magnetic field. Here we present the modeling results to derive all necessary parameters in equations (4) and (9). Simulations covered an energy range of 100 eV, 200 eV, 500 eV, 1000 eV,

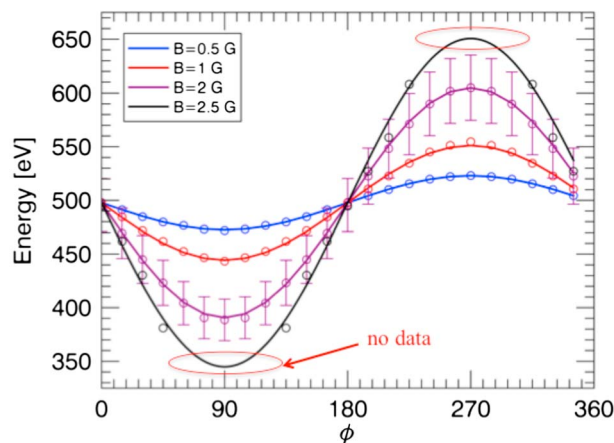


Figure 6. Energy response as a function of azimuth from simulation (circles) results and nonlinear best fits (curves) using equation (4). Four magnetic field strengths are shown: 0.5, 1, 2, and 2.5 G as blue, red, purple, and black curves, respectively. Error bars represent the ~10% FWHM of the simulated energy distribution.

deflected, thus striking different locations on the detector. The deviation depends on the ratio of B/\sqrt{E} and α . For example, when $\alpha = \pi/2$ then $\sin(\pi/2 - \alpha) = 0$, and $\beta = 0$. Thus, the Lorentz force bends the particle in the x - y plane regardless of its curved trajectory through the ESA. Likewise, the maximum deviation in β occurs when $\alpha = 0$ or π , which are measured outside the sensor. At these angles the force on the electron is initially zero; however, as the particle is guided along the spherical top hat geometry, the velocity and magnetic field are no longer parallel and this causes the electron’s azimuthal trajectory to bend.

Similar to the energy response, this ideal equation is unlikely to provide

2000 eV, and 5000 eV and magnetic fields of 0 G, 0.2 G, 0.5 G, 0.7 G, 1.0 G, 1.5 G, 2.0 G, 2.5 G, and 3.0 G. For each combination of energy and magnetic field strength, the azimuthal magnetic field component (i.e., ϕ) was rotated 360° in 15° increments. Similarly, the elevation (θ) was also simulated between 0° to +15° in 5° increments. A total number of ~2300 simulations were run to cover this parameter space, which totaled about 1000 h of computation time. Interactive Data Language (IDL) software was used to automate SIMION simulations through batch mode as well as automating data analysis routines to determine various ESA characteristics (e.g., voltage-angle response and detection response).

Amplitude Map vs. ESA Voltage and Magnetic Field

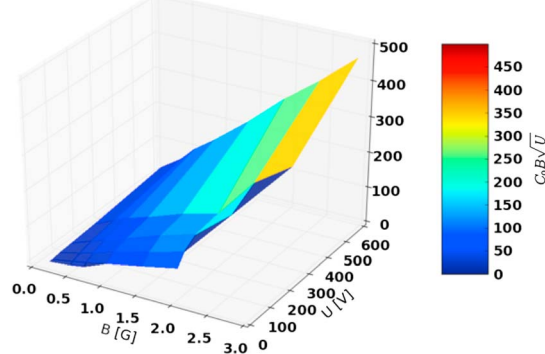


Figure 7. Amplitudes of equation (4) as a function of ESA voltage (U) and magnetic field strength (B). The free fitting parameter C_1 was determined by nonlinear least squares fitting routine to these data.

A nonlinear least square fitting routine was used to fit modeling results [Markwardt, 2009]. This routine was developed for IDL and uses the Levenberg-Marquardt method to minimize the chi-square (χ^2) goodness of the fit. It is possible during minimization of χ^2 that the fitting routine could be converging within local minima and not a global minimum as desired. To mitigate this effect, we supplied the fitting routine with initial guesses based off of the data and explored a reasonable range of initial guesses to be sure the fitting parameters converged to

the same values. We did not do this for every combination of energy and magnetic field strength and direction. Instead we spot-checked at 100, 500, and 1000 eV at 0° and 10° elevations for field strengths of 0.5, 1, 2, and 3 G. We determined that the program always found the same minimum for the cases provided, and thus, we have confidence the program properly converged over the whole parameter space.

To determine the errors of the fitting parameters in both the energy and pitch angle semiempirical models, we use the parabolic approximation around the minimum of χ^2 [Bevington and Robinson, 2003, and references therein]. This method was developed for nonlinear least squares fitting to an arbitrary function. For each fitting parameter a_j , we vary a_j slightly and calculate the change in χ^2 . Three points that straddle the minimum of χ^2 are fitted to a quadratic polynomial. Then the uncertainty in the fitting parameter is related to the second partial derivative of the quadratic fit by the following equation [Bevington and Robinson, 2003, equation 8.11]:

$$\sigma_j^2 = 2 \left[\frac{\partial^2 \chi^2}{\partial a_j^2} \right]^{-1} \tag{10}$$

4.1. Energy Response

Figure 6 illustrates the modeled central pass band energy response as a function of magnetic field azimuth for electrons with a uniform distribution of energy between ~ 300 to 700 eV. The ESA was held at a constant voltage of 55 V. The simulation results are plotted as circular symbols, and the solid curve represents the semiempirical fit using equation (4) where the C_0 fitting parameter was determined by the nonlinear fitting routine. For illustration purposes, error bars were only placed on the $B = 2$ G case, which we estimate to be $\sim 10\%$ based on the simulated energy resolution. The red ellipses mark regions on the 2.5 G case where there is no data due to the magnetic force being strong enough to prohibit transmission of particles through the ESA. As predicted by the semiempirical equations, the modeled energy response of JADE-E exhibits a periodic sine function with a constant offset. The equation fits the results well with reduced chi-square values typically near 0.5.

The amplitude of the sine function was calculated for all energy and magnetic field cases, as illustrated in Figure 7. The amplitude increases monotonically with increasing ESA voltage and magnetic field strength. We found the following relationship for C_0 representing the surface shown in Figure 7:

$$C_0 = (g_0 + B^{g_1}/U) \cos(\theta) \tag{11}$$

where g_0 primarily characterizes the slope of the term $B\sqrt{U}$ in equation (4) and the additional term B^{g_1}/U is needed for the sharp increases in the simulated amplitude for large B and small U . Lastly, $\cos(\theta)$ is needed

Parameter	Value	σ_j
g_0	6.4	0.6
g_1	5	1

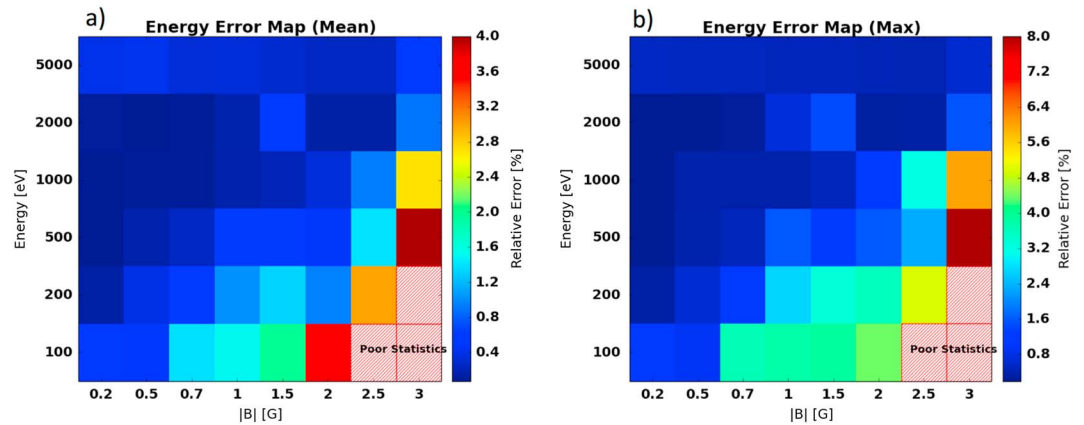


Figure 8. (a) Average relative and (b) maximum relative error between the energy model and simulation results as a function of energy and magnetic field strength. Areas with diagonal red lines represent regions with poor statistics.

to compensate for the magnetic field if it is not purely in the azimuthal plane. These terms were chosen empirically, and their best fit values are presented in Table 2. For example, in an extreme case where $B = 3$ G and $U = 11$ V, $B^{g_1}/U = 22$. In contrast, for $B = 1$ G and $U = 11$ V, $B^{g_1}/U = 0.09$. Some portions of the map (e.g., 100 eV at 2 G) appear to have blank or missing pixels. This was done to represent areas that do not have continuous data for $\phi = 0^\circ - 360^\circ$ (see Figure 6, $B = 2.5$ G case).

After the coefficients were derived for the energy model, we compared the semiempirical relationships to the simulation results and quantified the error. We report the error in terms of relative percent difference in energy (Figure 8). Some regions (e.g., 100 eV at 2.5 G) are not represented with errors and instead are labeled with “poor statistics.” This means that $\sim 80\%$ of the incident distribution did not transmit through the ESA. In general, the average error in Figure 8a is small ($< 2\%$) except for a few cases where the average error can grow to $\sim 4\%$. The maximum error map is organized very similar to the average errors, except here the error is nearly a factor of 2 larger. Typically the maximum error occurs around the peaks of the energy response (i.e., $\phi = 90^\circ$ and 270°). The energy response for various deflector settings was not explored as extensively as the $\beta = 0$ case. However, we did run simulations for 500 eV electrons in a 2 G field at $\beta = 15^\circ$ and $\beta = 30^\circ$

and found the average error to be $\sim 1\%$, respectively, a slight increase of the $\sim 0.5\%$ error found in Figure 8a.

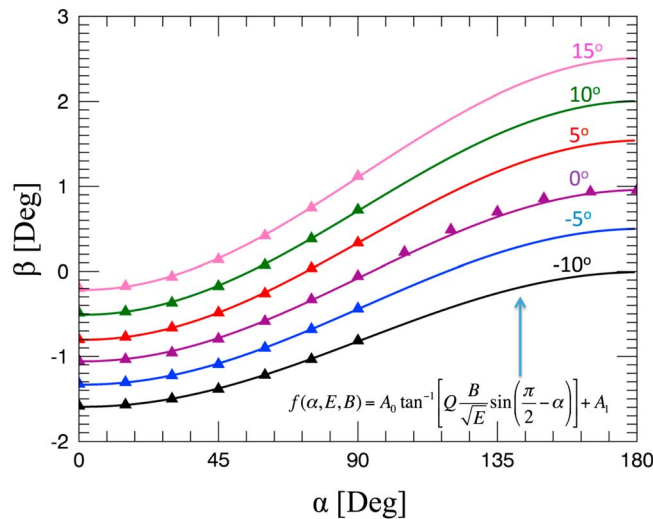


Figure 9. Detection angle on the MCP surface as a function of pitch angle outside the sensor for 1 keV electrons in a 1 G magnetic field. Symbols represent simulation data, and curves are nonlinear best fits using equation (9). Shown are multiple magnetic field elevation angles from -10° to $+15^\circ$.

4.2. Detection/Pitch Angle Response

Results in Figure 9 show the simulated detection location of 1 keV electrons in a 1 Gauss field as a function of the pitch angle outside the sensor. The symbols represent simulation results, and the curves are best fits using equation (9). Each color represents a different elevation angle. Here we chose to cover the full pitch angle range for the 0° case to illustrate the close symmetry between pitch angles $0^\circ - 90^\circ$ and from $90^\circ - 180^\circ$. For the other elevations shown we covered $0^\circ - 90^\circ$ pitch angles to reduce computation time. One striking feature is the effect due to the elevation of the magnetic field, which appears

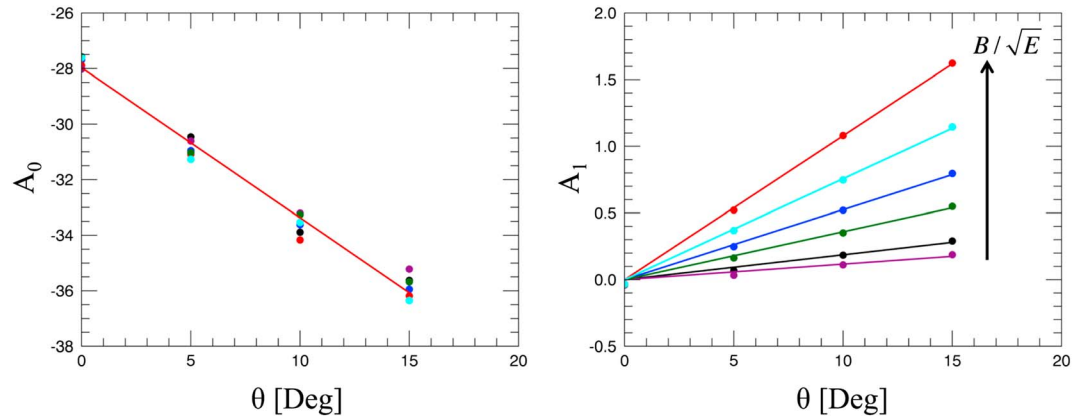


Figure 10. Plots of the fitting parameters A_0 and A_1 from equation (9). (left panel) A_0 as a function of elevation angle, and (right panel) A_1 as a function of elevation angle. Symbols represent simulation results, and curves are best fits.

to change the detection location on the MCP in a linear fashion with elevation angle. Over 25° elevation the detection location shifted $\sim 1.8^\circ$. For JADE-E this was within the azimuthal field of view (FOV) of 7.5° , but for stronger fields and/or lower energies this effect can shift the location larger than its FOV. However, these values change depending on the ESA design requirements. The amplitude, or A_0 , does not appear to shift substantially with elevation.

We explored various energies, magnetic field strengths, and elevations to find empirical relationships for the free fitting parameters in equation (9) (i.e., A_0 and A_1). A_0 did not show a systematic relationship with energy or magnetic field strength but did exhibit a linear relationship with elevation angle. Over the parameter space considered in this study, we found A_0 to cluster around a set of values, as shown in Figure 10a. Therefore, we were able to find a linear trend based on average values for the offset and slope. The red curve in Figure 10a illustrates that trend. Alternatively, A_1 showed systematic changes with energy, magnetic field strength, and elevation angle that could be characterized with a linear function (Figure 10b). Since all the offsets pass through $\sim 0^\circ$, with small variations ($< 0.05^\circ$), it was reasonable to neglect the vertical offset in the linear function and characterize only the slope. We found the slope could be characterized as multivariate polynomial of degree two with energy and magnetic field strength.

Presented in Table 3 are the values of each parameter that define the fitting function for detection location as a function of pitch angle. The relationships for fitting parameters A_0 and A_1 are given by

$$A_0 = a_0 + a_1\theta \tag{12}$$

$$A_1 = \left(a_2 \frac{B}{\sqrt{E}} \right) \theta \tag{13}$$

In Figure 11, the average and maximum error between the detection angle model and simulations are shown. Here we present the error in degrees. Similar trends as found in the energy model are also observed in Figure 11; the larger the ratio of B/U , the larger the difference between model and simulations. Generally, we can model the detection angle of an electron through the ESA, to better than $\sim 0.25^\circ$. However, in a couple of cases, the model can deviate as much as 0.4° . The maximum error is typically within 0.5° , except for the case of 200 eV electrons in a 2 G field, where the model is off by 0.8° . These values are reasonable given

the azimuthal FOV of JADE-E and other top hat ESA designs [e.g., Burch *et al.*, 2006; McFadden *et al.*, 2008; McComas *et al.*, 2013].

Table 3. Free Fitting Parameter Values and Uncertainties for the Detection Angle Model

Parameter	Value	σ_j
a_0	-27.9	0.6
a_1	-0.5	0.1
a_2	2.2	0.1

4.3. Geometric Factor Model

In Figure 6 we observed that certain conditions prevent the transmission of electrons through the ESA. This

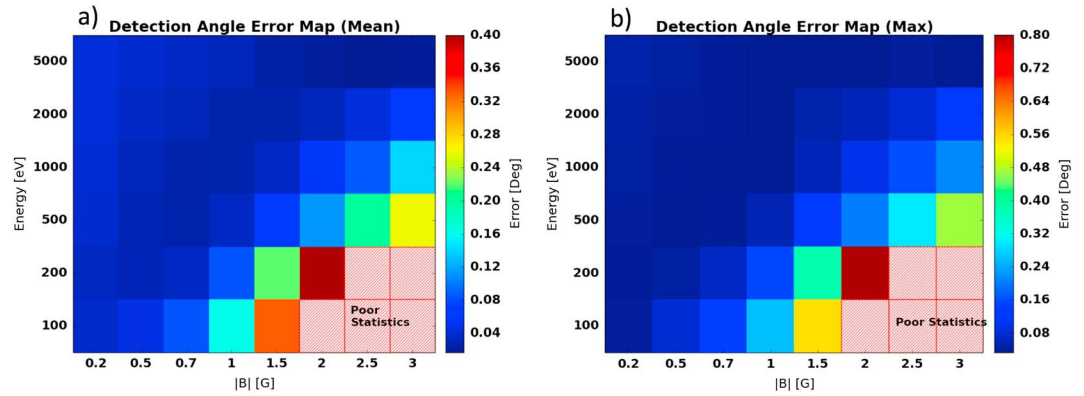


Figure 11. Error maps between the detection angle model and simulation results as a function of energy and magnetic field strength. (a) The average error and (b) the maximum error. Areas with poor statistics are represented as pixels with red diagonal lines.

directly affects the geometric factor—the quantity that relates count rate on the detector to particle flux outside the sensor. The simulated geometric factor can be calculated using a slightly modified expression from *McComas et al.* [2013]

$$G \cong \sum_{j=1}^{n_j} \sum_{i=1}^{n_i} \cos(\theta_j) \Delta\theta \Delta\varphi \Delta x \Delta z \frac{\Delta E}{E_i} T \quad (14)$$

$$T = \begin{cases} 1, & \text{if the electron strikes the MCP} \\ 0, & \text{if it does not} \end{cases} \quad (15)$$

where the solid angle of the FOV is $\cos(\theta)\Delta\theta\Delta\varphi$, the area is $\Delta x\Delta z$, and the energy resolution is $\Delta E/E$. The piecewise function T , describes whether or not a particle transmitted through the ESA. Typically, in laboratory experiments T may be defined as the ratio of incident particles to those detected.

The geometric factor expression is complex, and we did not derive a semiempirical relationship as we did with the previous models. Instead we found a Fourier series summed to $n=2$ and assuming it to be odd over the azimuthal domain of 0° and 360° does well in capturing the geometric function. The function can be written as

$$f(\varphi) = b_0 + \sum_{n=1}^2 b_n \sin(n(\varphi + \varphi_n)) \quad (16)$$

where b_0 is the offset, b_n are the amplitudes, n is the index, φ is azimuth (see Figure 3), and φ_n are constant phase shifts. We found from simulations that $\varphi_1 = 0^\circ$ and $\varphi_2 = 0.14^\circ$. Figure 12 illustrates the simulated G (equation (14)) as a function of azimuth for 500 eV electrons for various magnetic field strengths. Shown as circles are simulation results and solid curves are nonlinear best fits using equation (16). There are two main features of the geometric factor with increasing magnetic field: (1) the increasing amplitude of the sine functions and (2) the asymmetry with magnetic field azimuth direction. For the case shown, the geometric factor changes by approximately a factor of 50 over a few gauss. We only plot a range from 5×10^{-6} to 1×10^{-4} to highlight the features at $\varphi = 270^\circ$. The asymmetry in the geometric factor is likely due to the fact that as electrons are bent toward the inner

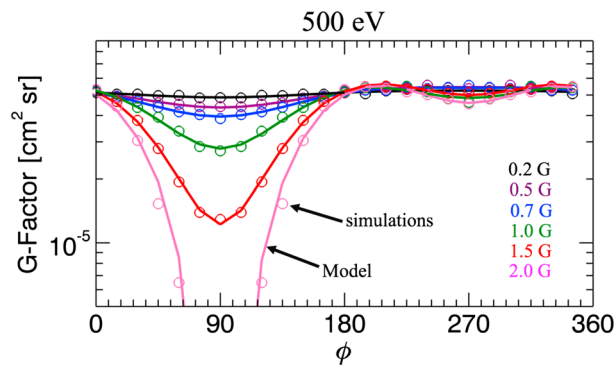


Figure 12. Geometric factor as a function of azimuth for 500 eV electrons in a varying magnetic field from 0.2 to 2.0 G. Circles represent simulation data, and the curves are fits using the Fourier model (equation (16)).

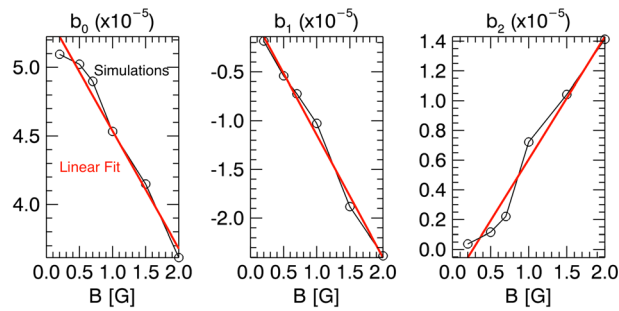


Figure 13. Free fitting parameters from equation (16) plotted as a function of magnetic field strength for 500 eV electrons. The black curve represents simulations and the red curve represents linear fits to the simulations. Best fit values for these parameters for all E and B can be found in equations (17)–(19).

are plotted in both E and B parameter space, they take the form of a curved surface, which we also found to be true in the previous semiempirical models (e.g., Figure 7). A nonlinear least squares fit to the Fourier fitting coefficients revealed the following relationships:

$$b_0 = 5.2 \times 10^{-5} - 1.8 \times 10^{-4} \frac{B}{\sqrt{E}} \tag{17}$$

$$b_1 = -3.2 \times 10^{-7} - 1.5 \times 10^{-4} \frac{B}{\sqrt{E}} \tag{18}$$

$$b_2 = -6.1 \times 10^{-7} + 1.7 \times 10^{-4} \frac{B}{\sqrt{E}} \tag{19}$$

5. Experimental Results

5.1. Laboratory Setup

For this study, all testing was performed in the Southwest Research Institute (SwRI) electron calibration facility [McComas *et al.*, 2013, Appendix A]. This facility has an ultra high vacuum chamber that is capable of reaching pressures as low as $\sim 10^{-10}$ Torr. In addition, there are two Kimball Physics electron guns that provide a

ESA, they then strike the surface and are either scattered or lost. However, when the electrons are bent toward the outer ESA, an increase in the electric field can offset this effect.

Likewise with the previous models, we characterized the coefficients of the Fourier series (Eqn. (16)) and found relationships that depend on incident particle energy (E) and magnetic field strength (B). Shown in Figure 13 are the free fitting coefficients b_0 , b_1 , and b_2 for the example in Figure 12. When the coefficients

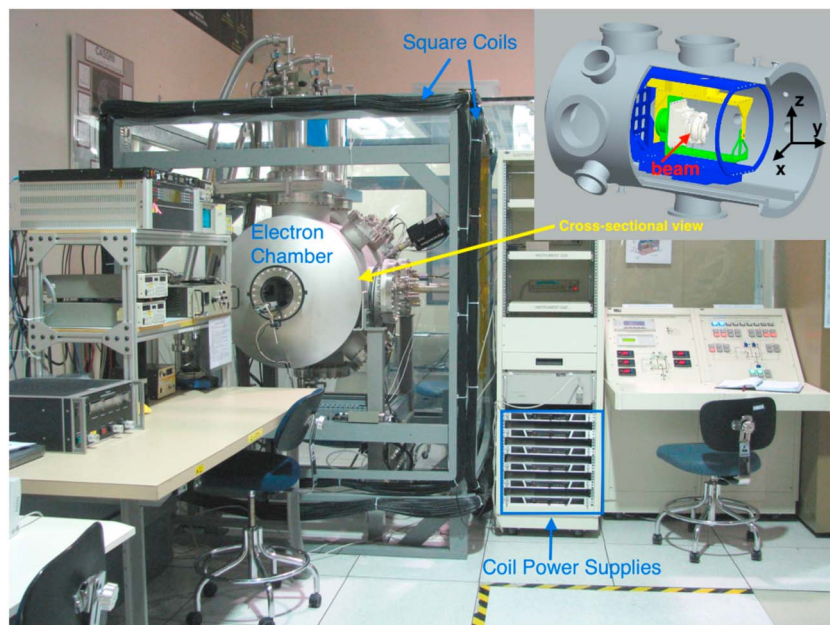


Figure 14. SwRI electron facility vacuum chamber and coils.

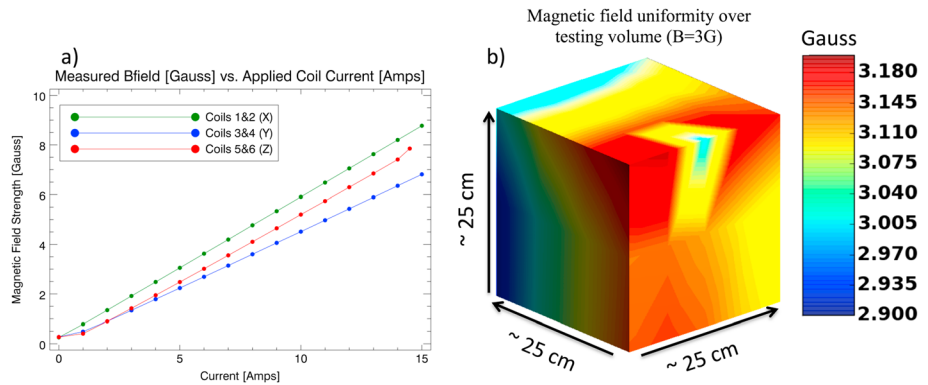


Figure 15. (a) Magnetic field strength and (b) magnetic field uniformity within the vacuum chamber. In Figure 15a the x, y, and z coils are represented by the green, blue, and red curves. In Figure 15b the uniformity is illustrated as a 3-D contour plot, with each side of the roughly cubic testing volume measuring at ~25 cm.

monoenergetic beam of electrons between 100 eV to 30 keV. Each electron gun is equipped with deflector plates and focusing optics to steer and manipulate the beam. Inside the chamber is a three-axis positioning system. These motions include a linear stage, which controls the horizontal position normal to the beam line and two nested, orthogonal rotational stages.

A set of square coils was fabricated and installed around the vacuum chamber in the electron facility (Figure 14). There are three sets of coils for three-axis control (x, y, and z coils are labeled in the Figure 14), which were

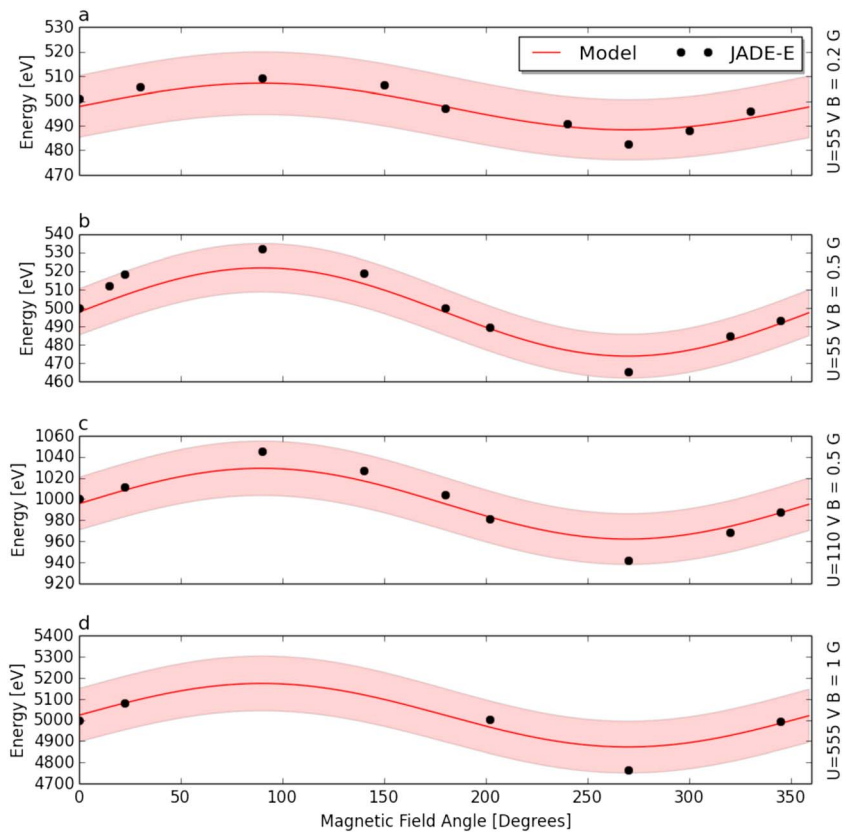


Figure 16. Measured and modeled energy as a function of magnetic field direction in the azimuthal plane (φ). Symbols represent JADE-E measurements, and the solid curves represent the semiempirical energy model. The semi-transparent swath represents a 2.5% variance from the model. (a) A 500 eV electrons in a 0.2 G magnetic field. (b) A 500 eV electrons in a 0.5 G field, (c) 1000 eV electrons in a 0.5 G field, and (d) 5000 eV electrons in a 1 G field.

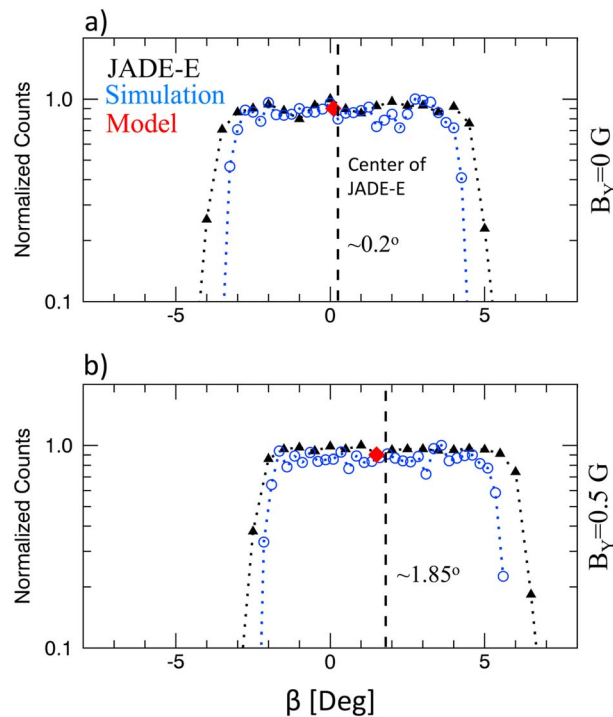


Figure 17. Normalized counts versus azimuth angle (φ) for 500 eV electrons with (a) $B_y = 0$ G and (b) $B_y = 0.5$ G. Black and blue curves represent JADE-E and simulation data respectively. The red diamond is the value calculated using equation (9) with defined values in Table 3. The vertical dashed line illustrates the azimuthal shift centered on the theoretical value.

magnetic field strength at 15 A for the x coils are ~9 G, ~7 G for the z coils, and ~8 G for the y coils. Each coil produces a slightly different magnetic field and varies slightly as a function of current. These differences are likely due to the size and location of the coils. A mounting plate was designed to attach to the motion stage to allow the magnetometer to be moved in ~2.5 cm increments over the full testing volume. Then the x coils were powered at a constant 5 A (i.e., 3 G), while measurements were taken. Figure 12b shows a 3-D continuous contour; therefore, interpolation was done between our 2.5 cm step sizes. Results in Figure 15b show that the magnetic field is spatially uniform to within <10% over the testing volume. It is likely that the presence of electromagnetic motors slightly skew the field. The design and development of coils around the SwRI electron calibration facility allow for the testing of an ESA in various magnetic field strengths and orientations.

5.2. Data Model Comparison

To test our modeling results, we performed a case study analysis with the JADE-E engineering unit. Using the coils, we varied the magnetic field direction while maintaining a constant magnitude to map out the energy as a function of magnetic field direction, as shown in Figure 16. Shown are results for 500 eV electrons in a 0.2 G and 0.5 G field, 1000 eV electrons in a 0.5 G field, and 5000 eV electrons in a 1 G field. All the aforementioned components of the magnetic field were purely in the azimuthal plane (i.e., the x-z plane in Figure 14). The symbols represent JADE-E data and the solid curves represent the semiempirical energy model based on simulation results. The swath represents a 2.5% variance of the semiempirical model to illustrate the error between the two. We note that strong values of B were not achievable in the electron chamber facility in this configuration. At values ~1 G and stronger, the trajectory of electrons within the gun and chamber were significantly altered and lost. Test setup alterations could have mitigated this problem, (i.e., new mounts for the gun or new motion stage for the sensor), but time constraints did not permit these changes. It is possible the calibration offsets used to convert the measured magnetometer signal to units of Gauss, may be off and explain the reason for the offset between the model and JADE-E (Figure 16). For example in the 1000 eV case, an increase of just 0.2 G would make the model and experiment agree to better than 0.5%. Although SIMION has been shown to represent JADE-E data well [McComas et al., 2013], it is also possible that some physical

designed to produce a nearly uniform (<10%) field over a ~25 x 25 x 25 cm³ test volume within the chamber. To achieve this, each coil is ~1.7 m in length with ~100 turns of wire that has a maximum current of 15 A. The setup was fabricated out of a wooden frame with wooden dowels to secure the coils to the frame. Aside from the electromagnetic stepping motors on the positioning system, the vacuum chamber is constructed out of nonmagnetic material. Inside the chamber, a three-axis Bartington magnetometer (MAG-03 IEHV) is mounted to the positioning system to map out the field strength and uniformity and to provide constant monitoring during tests.

Figure 15 illustrates the magnitude of the field for each coil pair as a function of current (a) and the uniformity of the field over the testing volume (b). To determine the magnitude, a magnetometer was placed in the center of the testing volume and the current was incremented by 1 A to a maximum of 15 A. The maximum

process is being overlooked which is producing this small error. However, in the cases shown the largest error is smaller than 2.5%. The energy resolution of JADE-E is $\sim 10\%$, so this error is reasonable.

Figure 17 shows the normalized counts as function of detection angle for 500 eV electrons with $B_Y = 0$ G (a) and $B_Y = 0.5$ G (b). The black and blue curves represent JADE-E and simulation results, respectively. The red diamond is the value calculated using equation (8) with the values defined in Table 3. In the lab it is not possible to track the exact position of an electron through the instrument; however, we can sweep the instrument in the imaging plane (i.e., ϕ) and calculate the center of the beam location based on where the counts fall off by a factor of 2. The calculated center position can then be compared to the value obtained by theory. It is apparent that a small shift is present in JADE-E for a 0.5 G field. The shift is also captured by our simulation data and compares well with our prediction from the semiempirical model (to within $\sim 0.25^\circ$). Simulation data does not capture the edge-to-edge response of the anode distribution and falls short by $\sim 1^\circ$. This may be because our SIMION model contains no gaps between the anodes, unlike that of the JADE-E detector.

6. Discussion and Summary

In this study we have investigated the effect of a strong external magnetic field on the response of a top hat electrostatic analyzer. Through extensive simulations, semiempirical relationships, and a case study analysis with JADE-E, we characterized the energy response, detection angle response, and the geometric factor. As expected from the Lorentz force with $B \neq 0$, simulations and experiment show that a strong magnetic field can alter the trajectory of electrons significantly and modify the energy, angle response, and the geometric factor of an ESA. This is because ESA voltages are typically optimized with $B = 0$. For example, 500 eV electrons in a 2 G field, the energy response is shifted by $\sim \pm 20\%$ depending on the field direction. However, with our work in this study, we show it is possible to work out the incident electron energy given knowledge of the ESA voltage, analyzer constant, magnetic field strength, and direction. The ESA voltages are controlled with flight software, the analyzer constant is known from calibration, and the magnetic field is typically measured with a magnetometer. Therefore, these independent variables in our model should be known.

The equations we presented in section 3 for the energy response and the pitch angle response have been shown to work well for energies between 0.1 keV to 5 keV with magnetic field strengths between 0 G to 3 G. It is currently unknown if a simple extrapolation of our semiempirical model beyond these values yields accurate results. The functions used to describe the amplitude and offset in our model are monotonic and perhaps could be extrapolated. However, one should be critical of the results.

The quantity $r\sqrt{k/2m}$ found in equation (3) (with added conversion factors going from nanoteslas to Gauss and eV to Joules) is equal to 4.49 for JADE-E. We replaced this quantity with the free fitting parameter C_0 , which we later found to be dependent on U and B (equation (11)). However, for fairly large gyroradii compared to the scale size of the instrument (e.g., $U > 50$ V and $B < 2$ G in JADE-E's case), then C_0 is at most about a factor of 2 larger than the quantity $r\sqrt{k/2m}$. Using this value instead, we observed the error to increase by a factor of ~ 2 in the energy error map. For example, for 500 eV electrons in a 2 G field, our model reproduced the energy distribution to within $\sim 1.5\%$ (see Figure 9), but using the quantity $r\sqrt{k/2m}$, it only increased to $\sim 3\%$. This suggests that our straightforward method in modeling the energy response of a top hat ESA can be applied to various other ESAs with different electro-optical characteristics and will yield relatively accurate results. For smaller voltages and larger magnetic field strengths, the differences become very large in a non-linear fashion. Thus, for accurate results we must rely on equation (4) with the functional form of C_0 .

The detection angle model presented in this study only depends on the ESA's diameter, which is a part of Q in equation (9). Unlike the energy model, where we could estimate the difference in using just the ESA's optical characteristics versus the modeled coefficients, we found that modeled coefficients are needed for all values of E and B to obtain accurate results in the detection angle. Regardless, we speculate that only a_0 in equation (12) may need to be characterized, since the other parameters depend on the elevation, kinetic energy, or magnetic field strength and not the properties of the ESA. Further testing with other instruments is needed to validate these claims.

We were not able to validate the geometric factor response to measurements with a top hat ESA. Future work is needed to setup an experiment that monitors the incident flux as a function of E and B , which is then compared to the measured count rate in the sensor. To do this accurately, one needs to measure the incident flux

Table 4. Regions of Interest, Associated Magnetic Fields and Energy Range of Concern for Electron Plasma Sensors

Region	$ \beta $ (nT)	$ \beta $ (G)	Energy Range of Concern for Electrons ^a
Solar wind	~ 5	$\sim 5 \times 10^{-5}$	None
Earth's ionosphere (100 km, 90° latitude)	$\sim 5 \times 10^4$	~ 0.5	<100 eV
Earth's equatorial magnetosphere ($5 R_E$)	~ 250	~ 0.0025	None
Jupiter's polar magnetosphere ($1 R_J$)	$\sim 2 \times 10^5$	~ 2	<1 keV
Jupiter's equatorial region ($5 R_J$)	$\sim 1 \times 10^4$	0.1	<5 eV
Jupiter's ionosphere (5000 km, 90° latitude)	$\sim 1.1 \times 10^6$	~ 11	<25 keV
Saturn's equatorial magnetosphere ($5 R_S$)	~ 100 nT	~ 0.001	None
Uranus' equatorial magnetosphere ($5 R_U$)	~ 200 nT	~ 0.002	None
Laboratory (San Antonio, TX)	$\sim 4 \times 10^4$	0.4	<100 eV

^aAssumes a radius of curvature of 5 cm (based on JADE-E).

with an absolute beam monitor [e.g., *Funsten et al.*, 2005] or Faraday cup. We note that our simulated geometric factor for JADE-E does compare well to the values reported in the JADE-E instrument paper [McComas *et al.*, 2013, Figure 51], which gives us confidence in our modeling approach. The offsets in fitting coefficients for the Fourier model (equations (17)–(19)) will need to be determined on a sensor-by-sensor basis, since each sensor has a unique geometric factor. But the framework has been laid out and the equations derived here can be used with the relevant parameters.

We expect these results to apply more to top hat ESAs, whether through direct use of the semiempirical relationships presented here or through the methodology used in deriving relationships to account for the electro-optical response in a magnetic field. One known application of this work will be to aid in data analysis of Juno JADE-E measurements. McComas *et al.* [2013, Figure 8] provided a histogram of magnetic field strengths that Juno is expected to encounter in the auroral regions of Jupiter, and they found that Juno is expected to be in regions where $B < 1$ G for 63.4% of the time, $B < 3$ G for 95.6% of the time, and $B < 5$ G for 99.2 % of the time. The equations provided in this study can be directly applied to the JADE-E data set to work out the energy, direction, and flux of the incident distribution of electrons, which is important for moment analysis. However, for regions where the magnetic field strength is larger than 3 G, these equations will have to be extrapolated to a parameter regime beyond that explored in this study.

Table 4 summarizes various regions of interest for plasma measurements and the expected magnetic field strength in that region. We define a range of energies that may be of concern for future missions with electron plasma sensors that are based on the strength of the magnetic field and the results with the JADE-E sensor. The ratio between the radius of curvature of the ESA and the gyroradius appears to be a decent indicator whether or not one can expect nonideal responses due to small electron gyroradii. We found the break point to be around 0.1, which is based on the electro-optical response differing by more than a few percent of the nonideal ($B = 0$) response. Values greater than 0.1 indicate that the external magnetic field may play a nonnegligible role in altering the response function of the sensor.

Acknowledgments

We are grateful to the Juno and JADE team members for making this work a possibility. We would also like to thank the following for their help with measurements, editing, or fruitful discussions on this topic (alphabetical order): Nick Alexander, Tom Broiles, Chelsea Clark, Dave Cronk, Rob Ebert, Austin Egert, Stefano Livi, Roberto Livi, Chad Loeffler, David Mackler, Paul Miles, Joey Mukherjee, Jillian Redfern, John Trevino, Phil Valek, and Scott Weidner. We also acknowledge the preliminary theoretical work done by the Harvey Mudd College (HMC) and for motivating further analysis, simulations, and experimental endeavors. Specifically, those apart of the HMC study that contributed are Ellis Cumberbatch, Kathleen Eliseo, Maxim Gibiansky, Joshua Kao, Vedika Khemani, Craig Pollock, Ethan Rubin, Rocio Rueles, Vatche Sahakian, and Mariam Youssef. We are also grateful for the helpful comments by Glyn Collinson and one other reviewer. Data supporting this work will be made available upon request. This work was carried out as a part of the JADE effort on the Juno mission, which is a part of NASA's New Frontiers Program.

References

- Allegrini, F., M. I. Desai, R. Livi, S. Livi, D. J. McComas, and B. Randol (2009), The entrance system laboratory prototype for an advanced mass and ionic charge composition experiment, *Rev. Sci. Instrum.*, *80*, doi:10.1063/1.3247906.
- Allegrini, F., M. I. Desai, S. Livi, D. J. McComas, and G. C. Ho (2014), The SupraThermal Ion Monitor for space weather predictions, *Rev. Sci. Instrum.*, *85*(5), 054501, doi:10.1063/1.4873327.
- Bagenal, F., et al. (2014), Magnetospheric science objectives of the Juno mission, *Space Sci. Rev.*, doi:10.1007/s11214-014-0036-8.
- Bevington, P. R., and D. K. Robinson (2003), *Data Reduction and Error Analysis*, 3rd ed., 320 pp., McGraw-Hill, New York.
- Burch, J. L., R. Goldstein, T. E. Cravens, W. C. Gibson, R. N. Lundin, C. J. Pollock, J. D. Winningham, and D. T. Young (2006), RPC-IES: The ion and electron sensor of the Rosetta plasma consortium, *Space Sci. Rev.*, *128*, doi:10.1007/s11214-006-9002-4.
- Carlson, C. W., and J. P. McFadden (1998), in *Measurement Techniques in Space Plasmas-Particles*, edited by R. F. Pfaff, J. E. Borovsky, and D. T. Young, pp. 125–140, AGU, Washington, D. C.
- Clark, G., F. Allegrini, B. M. Randol, D. J. McComas, and P. Louarn (2013), Response in electrostatic analyzers due to backscattered electrons: Case study analysis with the Juno Jovian Auroral Distribution Experiment-Electron instrument, *Rev. Sci. Instrum.*, *84*, doi:10.1063/1.4824352.
- Collinson, G. A., D. O. Kataria, A. J. Coates, S. M. E. Tsang, C. S. Arridge, G. R. Lewis, and R. A. Frahm (2009), Electron optical study of the Venus Express ASPERA-4 Electron Spectrometer (ELS) top-hat electrostatic analyser, *Meas. Sci. Technol.*, *20*, doi:10.1088/0957-0233/20/5/055204.
- Collinson, G. A., and D. Kataria (2010), On variable geometric factor systems for top-hat electrostatic space plasma analyzers, *Measur. Sci. Technol.*, *21*, doi:10.1088/0957-0233/21/10/105903.

- Collinson, G. A., et al. (2012), The geometric factor of electrostatic plasma analyzers: A case study from the Fast Plasma Investigation for the Magnetospheric Multiscale mission, *Rev. Sci. Instrum.*, *83*, doi:10.1063/1.3687021.
- Dahl, D. A. (2000), SIMION for the personal computer in reflection, *Int. J. Mass Spectrom.*, *200*(1–3), 3.
- Decreau, P., R. Prange, and J. J. Berthelier (1975), Optimization of toroidal electrostatic analyzers for measurements of low energy particles in space, *Rev. Sci. Instrum.*, *46*, doi:10.1063/1.1134412.
- Duvet, L., J. J. Berthelier, J. Illiano, and M. Godefroy (2000), A low-energy spectrometer with a 2π field of view for planetary missions, *Meas. Sci. Tech.*, *11*, doi:10.1088/0957-0233/11/4/306.
- Farnell, C. C., C. C. Farnell, S. C. Farnell, and J. D. Williams (2013), Electrostatic analyzers with application to electric propulsion testing, Electric Rocket Propulsion Society.
- Funsten, H. O., R. W. Harper, and D. J. McComas (2005), Absolute detection efficiency of space-based ion mass spectrometers and neutral atom images, *Rev. Sci. Instrum.*, *76*, 053301.
- Hughes, A. L., and V. Rojansky (1929), On the analysis of electronic velocities by electrostatic means, *Phys. Rev. Lett.*, *34*, 284, doi:10.1103/PhysRev.34.284.
- Johnstone, A. D. (1972), The geometric factor of a cylindrical plate electrostatic analyzer, *Rev. Sci. Instrum.*, *43*, doi:10.1063/1.1685826.
- Kasahara, S., K. Asamura, Y. Saito, T. Takashima, M. Hirahara, and T. Mukai (2006), Cusp type electrostatic analyzer for measurements of medium energy charged particles, *Rev. Sci. Instrum.*, *77*, doi:10.1063/1.2405358.
- Markwardt, C. B. (2009), Non-linear least squares fitting in IDL with MPFIT, in *Proc. Astronomical Data Analysis Software and Systems XVIII, Quebec, Canada, ASP Conference Series*, vol. 411, edited by D. Bohlender, P. Dowler, and D. Durand, pp. 251–254, Astronomical Society of the Pacific, San Francisco, Calif.
- McComas, D. J., J. E. Nordholt, J.-J. Berthelier, J.-M. Illiano, and D. T. Young (1998), *Measurement Techniques in Space Plasmas-Particles*, edited by R. F. Pfaff, J. E. Borovsky, and D. T. Young, pp. 201–235, AGU, Washington, D. C.
- McComas, D. J., et al. (2013), The Jovian Auroral Distribution Experiment (JADE) on the Juno Mission to Jupiter, *Space Sci. Rev.*, doi:10.1007/s11214-013-000-9.
- McFadden, J. P., C. W. Carlson, D. Larson, M. Ludlam, R. Abiad, B. Elliot, P. Turin, M. Marckwardt, and V. Angelopoulos (2008), The THEMIS ESA plasma instrument and in-flight calibration, *Space Sci. Rev.*, *141*, doi:10.1007/s11214-008-9440-2.
- Paschmann, G., H. Loidl, P. Obermayer, M. Ertl, R. Laborenz, N. Sckopke, W. Baumjohann, C. W. Carlson, and D. W. Curtis (1985), The plasma instrument for AMPTE IRM, *IEEE Trans. Geosci. Remote Sens.*, *GE-23*, doi:10.1109/TGRS.1985.289525.
- Pollock, C. J., V. N. Coffey, J. D. England, N. G. Martinez, T. E. Moore, and M. I. Adrian (1998), *Measurement Techniques in Space Plasmas-Particles*, edited by R. F. Pfaff, J. E. Borovsky, and D. T. Young, pp. 201–235, AGU, Washington, D. C.
- Randol, B. M., R. W. Ebert, F. Allegrini, D. J. McComas, and N. A. Schwadron (2010), Reflections of ions in electrostatic analyzers: A case study with New Horizons/Solar Wind Around Pluto, *Rev. Sci. Instrum.*, *81*, doi:10.1063/1.3499367.
- Risley, J. S. (1970), Magnetic field measurements using an electron beam and an electrostatic analyzer, *Rev. Sci. Instrum.*, *42*, doi:10.1063/1.1685066.
- Sablík, M. J., D. Golimowski, J. R. Sharber, and J. D. Wittingham (1988), Computer simulation of a 360° field-of-view “top-hat” electrostatic analyzer, *Rev. Sci. Instrum.*, *59*, doi:10.1063/1.1139991.
- Toburen, L. H., and W. E. Wilson (1977), Energy and angular distributions of electrons ejected from water vapor by 0.3–1.5 MeV protons, *Rev. Sci. Instrum.*, *66*, doi:10.1063/1.433783.
- Wadey, W. G. (1956), Magnetic shielding with multiple cylindrical shells, *Rev. Sci. Instrum.*, *27*, doi:10.1063/1.1715413.
- Wolfe, J. H., R. W. Silva, and M. A. Myers (1966), Observations of the solar wind during the flight of Imp 1, *J. Geophys. Res.*, *71*, 1319–1340, doi:10.1029/JZ071i005p01319.
- Young, D. T., A. G. Ghielmetti, E. G. Shelley, J. A. Marshall, and J. L. Burch (1987), Experimental tests of a toroidal electrostatic analyzer, *Rev. Sci. Instrum.*, *58*, doi:10.1063/1.1139260.
- Young, D. T., S. J. Bame, M. F. Thomsen, R. H. Martin, J. L. Burch, J. A. Marshall, and B. Reinhard (1988), 2π -radian field-of-view toroidal electrostatic analyzer, *Rev. Sci. Instrum.*, *59*, doi:10.1063/1.1139821.
- Young, D. T., R. P. Bowman, R. K. Black, T. L. Booker, P. J. Casey, G. J. Dirks, D. R. Guerrero, K. E. Smith, J. H. Waite Jr., and M. P. Wüest (1998), *Measurement Techniques in Space Plasmas-Particles*, edited by R. F. Pfaff, J. E. Borovsky, and D. T. Young, pp. 313–318, AGU, Washington, D. C.
- Victor, A. L., T. H. Zurbuchen, and A. D. Gallimore (2006), Top hat electrostatic analyzer for far-field electric propulsion plume diagnostics, *Rev. Sci. Instrum.*, *77*, doi:10.1063/1.2165549.
- Vampola, A. L. (1998), *Measurement Techniques in Space Plasmas-Particles*, edited by R. F. Pfaff, J. E. Borovsky, and D. T. Young, pp. 339–355, AGU, Washington, D. C.